



**HAL**  
open science

# 3D characterization of the propagation of liquid metal embrittlement inner cracks during tensile shear testing of resistance spot welds

Outhmane Siar, Sylvain Dancette, Jérôme Adrien, Thomas Dupuy, Damien Fabrègue

## ► To cite this version:

Outhmane Siar, Sylvain Dancette, Jérôme Adrien, Thomas Dupuy, Damien Fabrègue. 3D characterization of the propagation of liquid metal embrittlement inner cracks during tensile shear testing of resistance spot welds. *Materials Characterization*, 2021, pp.111664. 10.1016/j.matchar.2021.111664 . hal-03471233

**HAL Id: hal-03471233**

**<https://hal.science/hal-03471233>**

Submitted on 26 Sep 2022

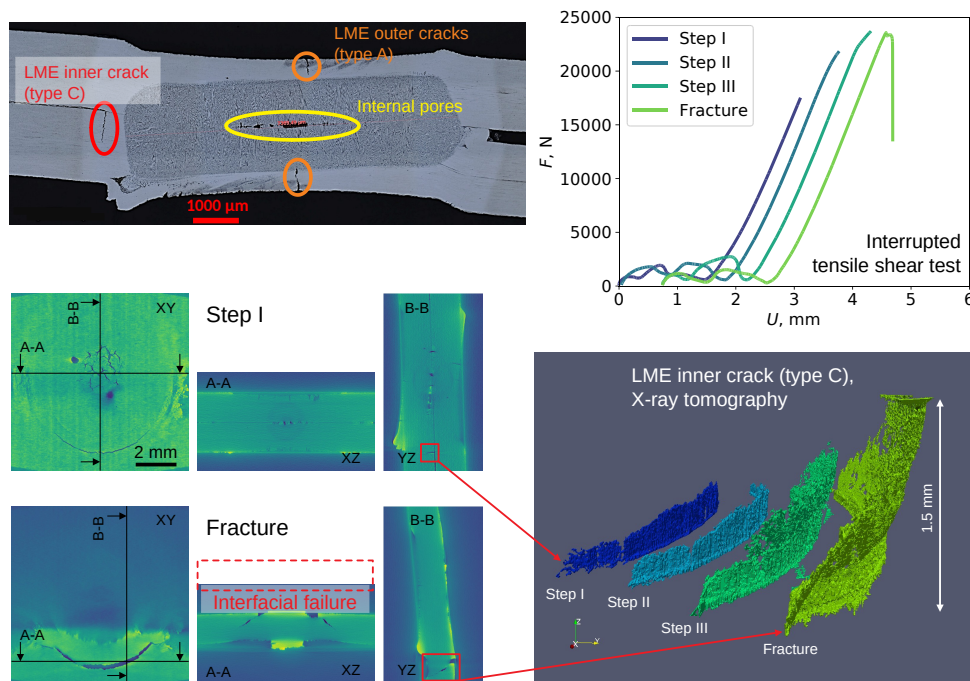
**HAL** is a multi-disciplinary open access archive for the deposit and dissemination of scientific research documents, whether they are published or not. The documents may come from teaching and research institutions in France or abroad, or from public or private research centers.

L'archive ouverte pluridisciplinaire **HAL**, est destinée au dépôt et à la diffusion de documents scientifiques de niveau recherche, publiés ou non, émanant des établissements d'enseignement et de recherche français ou étrangers, des laboratoires publics ou privés.

# Graphical Abstract

## 3D characterization of the propagation of liquid metal embrittlement inner cracks during tensile shear testing of resistance spot welds

Outhmane Siar, Sylvain Dancette, Jérôme Adrien, Thomas Dupuy, Damien Fabrègue



# 3D characterization of the propagation of liquid metal embrittlement inner cracks during tensile shear testing of resistance spot welds

Outhmane Siar<sup>a,b</sup>, Sylvain Dancette<sup>a</sup>, Jérôme Adrien<sup>a</sup>, Thomas Dupuy<sup>b</sup>,  
Damien Fabrègue<sup>a</sup>

<sup>a</sup>*Univ Lyon, INSA Lyon, CNRS UMR5510, Laboratoire  
MATEIS, Villeurbanne, F-69621, France*

<sup>b</sup>*ArcelorMittal Global R&D, Voie Romaine, Maizières-lès-Metz, F-57283, France*

---

## Abstract

An X-ray tomography setup is developed in this work in order to characterize liquid metal embrittlement (LME) cracks and internal defects in 3D in homogeneous advanced high strength steel resistance spot welds, non destructively. For the first time, the propagation of the LME inner crack could be monitored in the course of *ex situ* tensile shear loading. While propagating in a stable way through the sheet thickness in the vicinity of the weld nugget, the LME inner crack does not modify the final fracture path, all investigated welds failing at the faying surface (full interfacial failure type).

*Keywords:* advanced high strength steels, resistance spot welds, type C LME crack, X-ray tomography, tensile shear

---

## 1. Introduction

Over the past decades, advanced high strength steels (AHSS) were developed for the automotive industry, allowing to achieve tensile strength levels up to 1500 MPa in the case of steel grades designed for cold forming. Among these, 3<sup>rd</sup> generation AHSS (also called TRIP-aided AHSS) use a rather high alloying element content and contribute to the reduction in weight of car structures while improving their crashworthiness. Zinc coating is often used to protect AHSS from external corrosion (Marder [1]).

Resistance spot welding (RSW) is the most used joining process for automotive structures. However, the combination of high alloying content and

zinc coating makes it often challenging in the case of AHSS (Beal et al. [2], Jeon et al. [3]). Indeed, the liquid metal embrittlement (LME) phenomenon may occur due to the low melting point of zinc (420 °C) and the high temperature and stress state arising during the RSW process. In such case, liquid zinc penetrates in the steel matrix through the grain boundaries and may induce grain boundary decohesion (LME cracks).

LME cracks were classified into two main categories depending on their location: *outer* cracks located at the weld surface and *inner* cracks located in the vicinity of the notch tip at the faying surface [4]. This is illustrated in Figure 1. Note that *outer* cracks are usually further subdivided into type A and B cracks depending on their location with respect to the indentation shoulder of the electrode. *Inner* cracks correspond to type C in this classification.

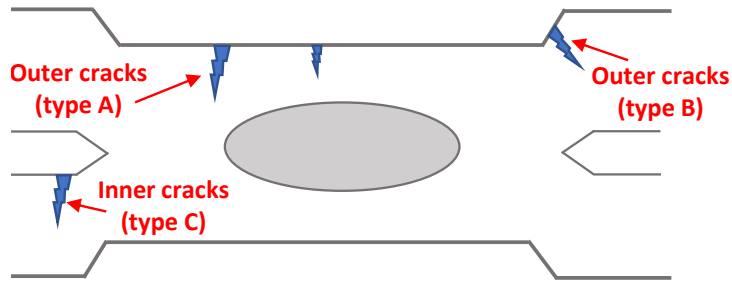


Figure 1: LME inner cracks and outer cracks according to AWS [4].

The influence of LME cracks on the mechanical behavior of AHSS spot welds is still debated in the literature and hinders the spread of some new generation AHSS in the automotive industry.

In the case of LME *outer* cracks, Gaul et al. [5], Brauser et al. [6], Kim et al. [7] showed that the fatigue life of spot welds was not significantly affected by the presence of the cracks. Choi et al. [8] showed that small LME outer cracks (< 500 microns) in TRIP spot welds would not induce significant loss of cross tension strength, absorbed energy and fatigue life, while longer crack could. Similar conclusions were found by DiGiovanni et al. [9] in tensile shear. Benlatreche et al. [10, 11] showed that LME outer cracks as deep as half the sheet thickness would not propagate from the surface, neither in cross tension, tensile shear, nor during fatigue or crash testing.

Until very recently (Siar et al. [12], Kwon et al. [13]), such experimental

evidence did not exist in the literature in the case of LME *inner* cracks. As a matter of fact, their occurrence is rare compared to *outer* cracks (Siar et al. [14]) and the monitoring of their evolution during a mechanical test is difficult. However, they may be seen as the most dangerous LME cracks since they appear close to the notch tip at the faying surface between the two sheets, a well known point of fracture initiation in resistance spot welds (Bouzekri et al. [15], Dancette et al. [16, 17], Huin et al. [18]).

One of the biggest problems when studying the impact of LME cracks during mechanical testing concerns the detection and characterization of the cracks before and during the test. Nowadays, LME cracks characterization is often made by (destructive) metallographic cross sections in the welds (Benlatreche et al. [19]), providing only a partial view of the 3D crack morphology. Because the crack depth is usually not uniform through the weld, the observed severity of the crack depends on the selected cutting plane (DiGiovanni et al. [20]). Improper choice of the plane of observation might lead to a misunderstanding of LME severity. Furthermore as LME is a heterogeneous and dispersive phenomenon, spot welds obtained under the same welding conditions may present varying number and size of LME cracks (Benlatreche et al. [19], Bhattacharya [21], Siar et al. [14]). Therefore, the confirmation of the presence and severity of LME cracks in mechanically loaded samples can only be performed *post mortem* with the metallography technique. This prevents a clear description and understanding of the evolution of the critical LME crack during mechanical loading, as well as of its actual contribution (or absence of contribution) to the final fracture path.

X-ray computed tomography emerged in the last decades as a reference technique to analyze the failure mechanisms of materials in three dimensions (3D) (Maire and Withers [22]). As a non destructive technique, it allows for *in situ* testing of materials in a wide range of loading conditions (Buffiere et al. [23]). Although a few works have initiated very recently the use of X-ray tomography to quantify the characteristics of LME cracks (Hang et al. [24]), no study can be found in the literature regarding the use of this non-destructive technique to monitor the evolution of LME cracks in resistance spot welds and assess their impact on the weld fracture.

In the present work, we present for the first time a detailed analysis of the 3D evolution of LME inner cracks during the tensile shear testing of spot welds, imaged by X-ray tomography. This is carried out on homogeneous resistance spot welds made of a 3<sup>rd</sup> generation AHSS, using controlled and severe deterioration of the welding parameters to favor the occurrence of

LME inner cracks in a reproducible way (Siar et al. [14, 12]). Section 2 in the following describes the experimental procedure, after which the results are presented in section 3 and discussed in section 4 before a short summary of the main findings.

## 2. Materials and methods

### 2.1. Sample preparation

The material investigated in this study is a carbide free bainite (CFB) steel (3<sup>rd</sup> generation AHSS) with the chemical composition detailed in Table 1.

C	Si	Mn	P	S	Cr	Ti	B
0.231	1.43	2.08	0.015	0.0006	0.351	0.008	0.0006

Table 1: Chemical composition of the investigated steel grade (wt.%).

All sheets are 1.56 mm thick and electro-galvanized with a 7.5 microns pure Zn layer. This steel exhibits a good combination of strength and ductility with a yield strength of 1000 MPa, a tensile strength of 1200 MPa and an elongation of about 14%. At room temperature, its microstructure is made of a bainitic matrix containing small quantities of martensite and residual austenite.

Two-sheet homogeneous resistance spot welding was performed. 150 mm  $\times$  25 mm  $\times$  1.56 mm coupons were cut from the steel sheet and welded in the tensile shear configuration with a 50 mm overlap (Figure 2).

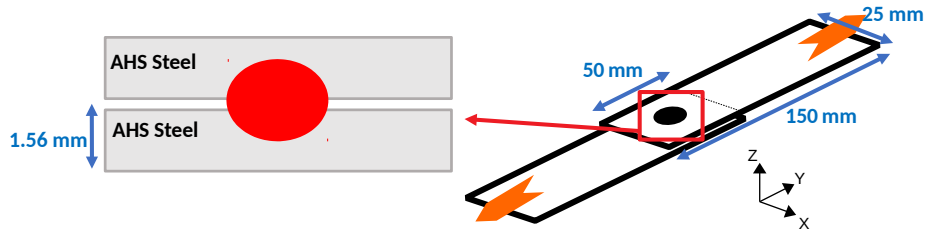


Figure 2: Tensile shear configuration investigated.  $X - Y$  plane corresponds to the sheet plane and  $Z$  corresponds to the sheet thickness direction throughout the paper. Load is applied in the  $Y$  direction.

This homogeneous configuration, both in terms of steel grade and sheet thickness, was chosen to quantify the intrinsic behavior of the material without the influence of a second sheet (with either different apparent stiffness or yield strength depending on steel grade and sheet thickness).

Samples were welded using a 50 Hz AC pedestal resistance spot welding machine with F1-16-20-50-6 electrodes (ISO5821 [25]). All the welds investigated in this study were produced using specific welding parameters, severely deteriorated compared to ISO standards to promote the occurrence of LME inner cracks. These were identified in a previous study, i.e. short holding time, electrode misalignment and maximum welding current intensity (Siar et al. [14]). The welding parameters used compared to the standard ones for the present weld configuration are presented in Table 2. Deviations from the standard are highlighted in bold. These deteriorated welding conditions allow to produce systematically one and only LME inner crack in the weld.

	Misalignment	Welding time	Electrode force	Holding time	Welding current
Inner LME	<b>5°</b>	380 ms	4.5 kN	<b>20 ms</b>	$I_{max}$
ISO	0°	380 ms	4.5 kN	260 ms	$I_{max}$

Table 2: Welding parameters for the occurrence of LME inner cracks compared to ISO-18278-2 standard.

The particular symmetry of the tensile shear specimen (Figure 2) combined with electrode misalignment and the presence of a single LME inner crack allows one to distinguish two cases illustrated in figure 3.a and 3.b:

- Loaded-crack sample (Figure 3.a): the LME inner crack is located on the side of the sheet that will be directly subjected to the tensile shear load.
- Unloaded-crack sample (Figure 3.b): the LME inner crack is located on the loose end of the sheet, opposite to the tensile shear load.

In order to maintain a misalignment of 5° between the sheets and the electrodes during welding (Figure 3), a special sample holder was used (see also Siar et al. [14]). It introduces a slight asymmetry of mechanical constraints in the two sheets, one sheet being clamped while the other is only guided in the proper direction. As a consequence, the inner LME crack always appeared in the most constrained sheet. This allowed to anticipate on which side of the assembly the inner LME crack would appear and position

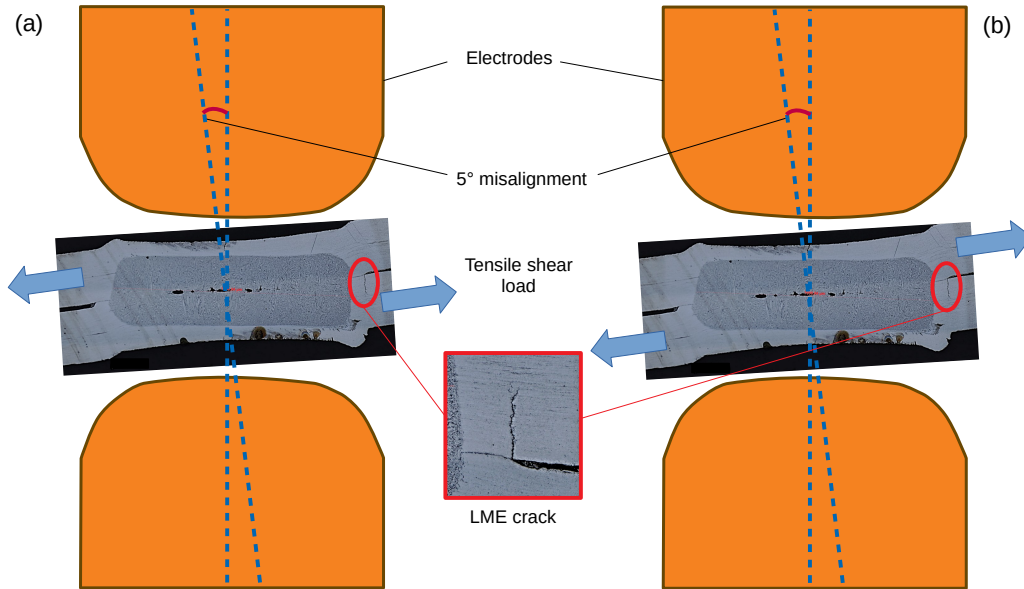


Figure 3: Two configurations of the samples and LME inner crack with respect to loading: a) loaded-crack, b) unloaded-crack. Note that the tensile shear test (schematically indicated by blue arrows) was performed subsequent to resistance spot welding.

it in the desired loaded or unloaded configuration during the tensile shear test. Figure 3 further illustrates that the effect of electrode pressure and misalignment produces a bump at the exterior surface of the weld metal, close to the end of the region in contact with the electrode tip. The LME inner crack is located in the vicinity of the bottom bump (i.e. the larger one), on the interior side of the sheet.

## 2.2. X-ray microtomography

X-ray tomography allows to reconstruct the 3D volume from 2D projections of the specimen rotating under the x-ray beam. Acquisitions were carried out using a Phoenix X-ray vto me xs laboratory tomograph equipped with a 160 kV nano-focus tube, a tungsten transmitting target and a  $1920 \times 1536$  pixels Varian detector. The device was operated at 140 kV and  $80 \mu\text{A}$  current, with a 0.3 mm copper filter. The voxel size was set to 7 microns. A full scan consisted of 1200 projections (0.667 s exposure time, averaging 3 images) recorded under a  $360^\circ$  rotation of the specimen. The volumes were reconstructed by a filtered back projection Feldkamp-algorithm.

Under these conditions, the transmission was largely sufficient when the

X-ray beam passed through the 3.12 mm thickness of two sheets, but became very low when the sample was rotated at 90° with the 25 mm sample width aligned with the beam axis. These results in reconstructed slices are a little noisier and blurred compared to an acquisition where the transmission is constant and sufficient on all projections. However, the volumes obtained allow to highlight the presence of cracks and pores within the specimens.

The 3D scans were analyzed using the Fiji software (Ferreira and Rasband [26]) and segmentation was performed using the seeded region growing technique. 3D views were obtained with the Paraview software (Squillacote [27]).

### 2.3. *Ex situ mechanical testing*

Mechanical tests were carried out on an Instron 5967 tensile machine. A 30 kN load cell was used and the crosshead displacement was controlled at a rate of 5 mm/min.

Interrupted tensile shear tests were performed on the loaded-crack and unloaded-crack specimens, until final fracture. In the initial state and after each interruption, the sample was removed from the tensile machine and a tomography scan was performed to characterize the 3D morphology of the LME inner crack. This *ex situ* testing procedure allows to monitor the evolution of the same crack from the beginning of the test up to final fracture. Three loaded-crack and two unloaded-crack samples were investigated in this way.

## 3. Results

### 3.1. *Destructive and non-destructive characterization of spot welds*

Figure 4 shows a typical metallographic cross section through the center of the weld. The welding parameters of Table 2 produce welds with an average nugget diameter of 7.1 mm (standard deviation 0.1 mm) measured on the five samples subjected to tomography scanning.

One can observe several defects in the welds, which were systematically observed in all welds investigated: (i) the center of the weld nugget contains internal pores resulting from the solidification of the weld pool, (ii) small LME outer cracks (type A) can be seen at the exterior surfaces of the weld nugget and (iii) one LME inner crack (type C) is present in the vicinity of the notch tip, on one side of the weld nugget. Note that the LME inner crack

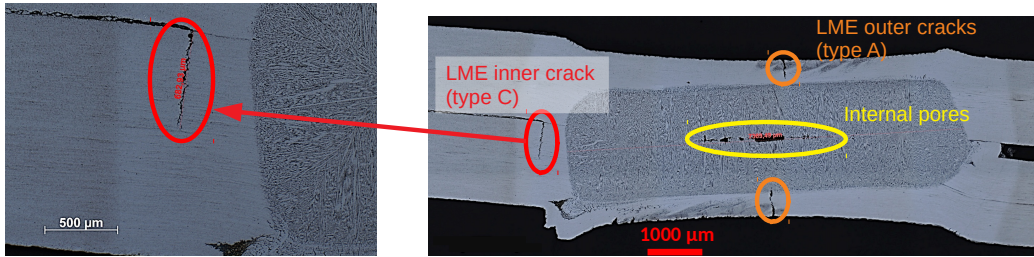


Figure 4: Metallographic cross section.

is always located close to the most pronounced metal bump produced by the misaligned electrode.

One advantage of X-ray tomography over (destructive) metallographic cross section is the ability to characterize these defects non-destructively and in 3D. This is illustrated in Figure 5, showing the 3D reconstruction of the different types of defects in a resistance spot weld. Figures 5.a-c are 2D slices in the 3D volume of the weld. The  $XY$  plane, passing close to the faying surface, depicts some of the internal pores in the center of the weld as well as an overview of the LME inner crack on the bottom side of the image. The A-A ( $XZ$  plane) and B-B ( $YZ$  plane) cross sections depict the extent of defects in the thickness direction.

Moreover, 3D views of the segmented internal pores, outer cracks and inner crack are provided in Figures 5.d-f. The color code highlights the number of 3D disconnected features (labels) in these views, namely 40 internal pores of varying size, 16 features in the LME *outer* cracks and 1 LME *inner* crack. Note that the segmentation procedure, depending on image resolution and contrast, may artificially separate different parts of a given object. This seems to be the case for the LME *outer* cracks, where one could imagine a continuous network of branching cracks while they appear disconnected in Figure 5.d. One should note that the volume of Figure 5 was reconstructed after the first load step of the tested sample. In the initial scan of the sample (before loading), the thin LME *inner* crack could not be clearly detected using the present tomography setup (7 microns voxel size), while the slight opening of the loaded crack at the first load step allowed to detect it unambiguously.

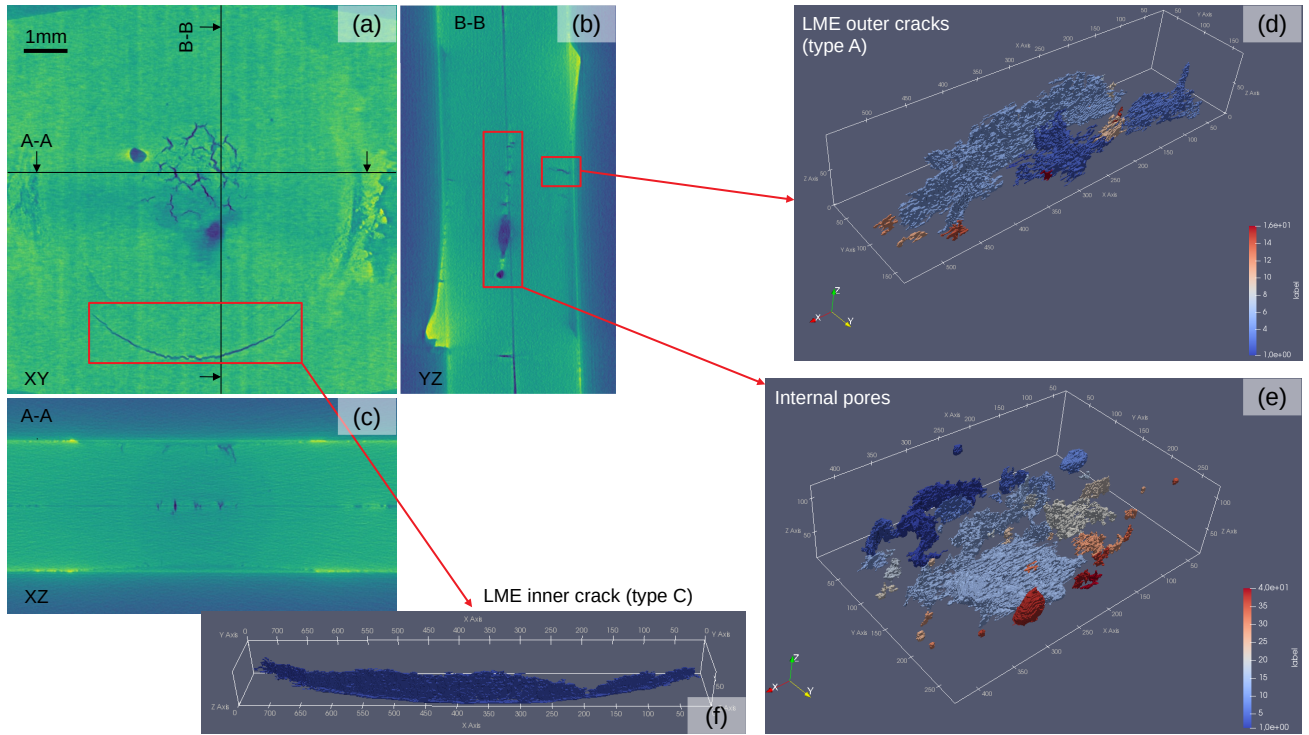


Figure 5: Loaded-crack sample at the first load step of 17.4 kN, as reconstructed from X-ray tomography. a-c) Slices in the weld volume and d-f) 3D views of the different types of defects.  $XY$ ,  $XZ$  and  $YZ$  planes refer to the reference frame depicted in Figure 2.

### 3.2. Loaded-crack samples

Figure 6 exhibits the evolution of a weld with a loaded crack (Figure 3) under *ex situ* loading. All loaded-crack samples investigated in this study followed a similar sequence of damage evolution, leading to a final fracture of the weld at the faying surface (full interfacial failure), independently of any of the LME cracks.

Figure 6 focuses on the evolution of the LME inner crack, all other defects in the weld (internal pores or outer cracks at the exterior surface) remaining unaffected during loading.  $XY$ ,  $XZ$  and  $YZ$  slices in the 3D volume of the weld are shown at the four levels of load interruption depicted in the force-displacement curves of Figure 6.e. Figure 6.f shows a 3D view of the evolving LME inner crack at the increasing load steps. The opening of the LME inner crack can be seen in Figures 6.a-d from the  $XY$  slices. Lateral views in the  $XZ$  and  $YZ$  slices in Figures 6.c-d illustrate the radial opening

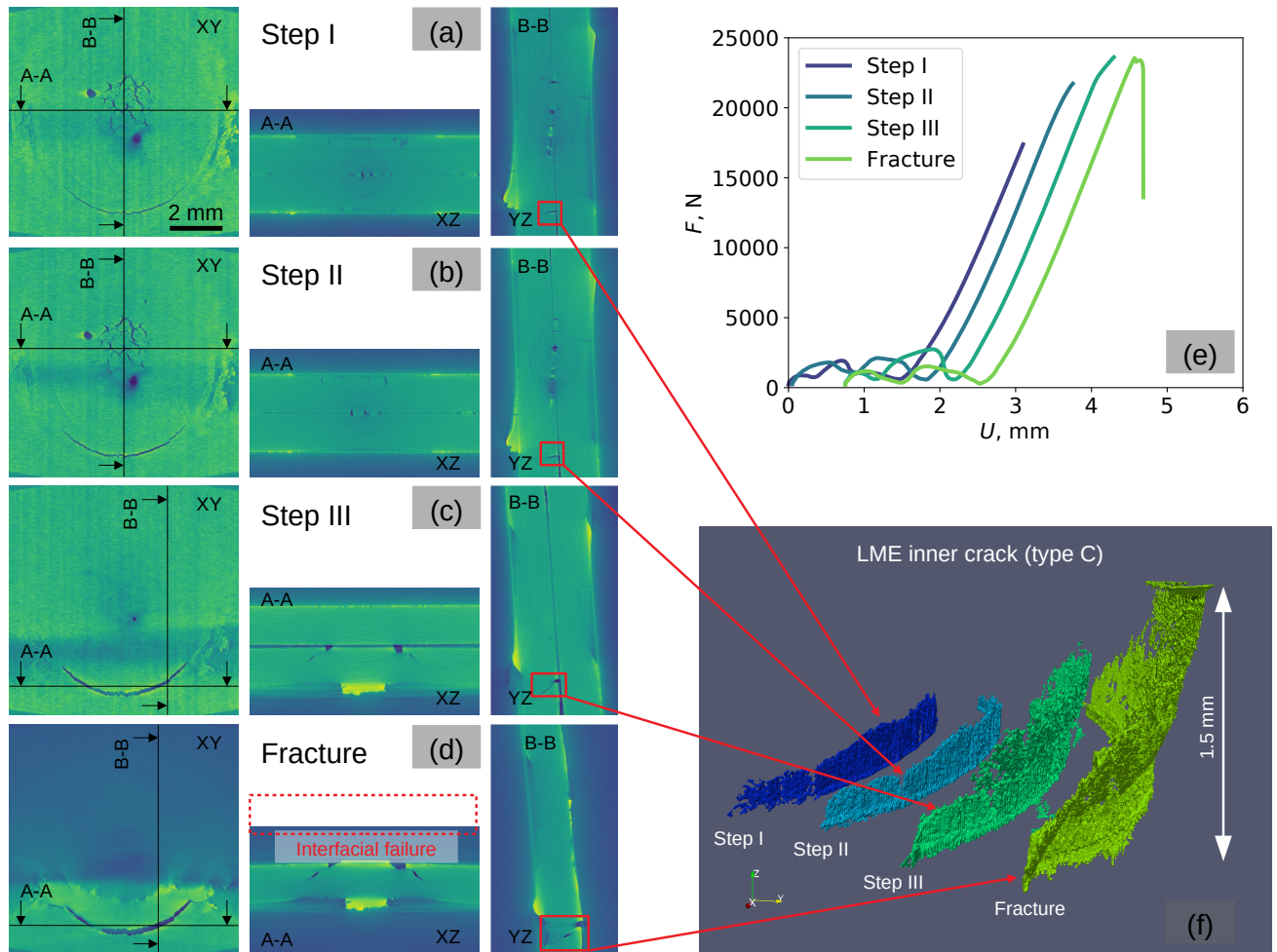


Figure 6: Loaded-crack sample. a-d) Slices in the tomography volumes at increasing load levels. e) Interrupted loading curves depicting the increasing load steps, where the curves are virtually shifted from each other for better readability. f) 3D rendering of the LME *inner* crack during loading. Final fracture occurs by full interfacial failure independently of the observed LME cracks.

and deviation of the crack as it is propagating through the sheet thickness at the higher load levels. One can also note the global rotation of the weld in the  $YZ$  slices as a result of the bending moment operating in the tensile shear specimen, where the load vectors in the two sheets are in opposite directions and separated by a lever arm corresponding to the sheet thickness. The 3D view of Figure 6.f gives a closer look at the crack advance through the sheet

thickness.

The contours of the LME inner crack are further illustrated in Figure 7, where the crack was projected in the  $XZ$  plane for easier representation in 2D.

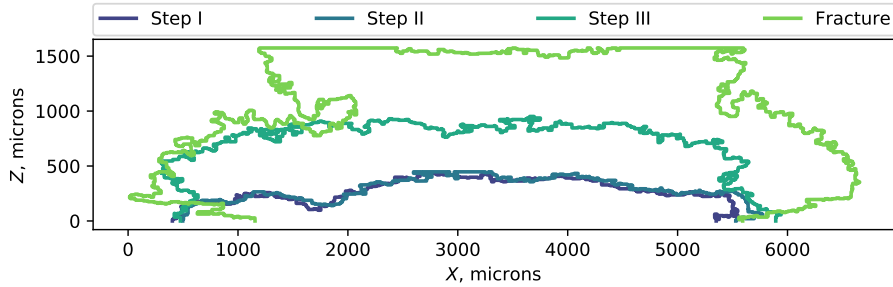


Figure 7: Contours of the LME inner crack propagation during loading, projected in the  $XZ$  plane perpendicular to the load direction.

Figures 6.f and 7 show the absence of propagation of the LME crack for most of the load bearing capacity of the weld. Namely, the crack front did not advance up to Step II (21.7 kN) while the peak load  $F_{max}$  of the weld reached 23.6 kN. Significant propagation of the crack occurred later from Step III until final fracture, where the crack reached the outer surface of the weld. Nevertheless, limited angular extension of the LME inner crack is observed in Figures 6.f and 7 from the initial state to final fracture. As a final comment regarding this sample, it is important to note that the LME inner crack did not contribute to the final fracture surface of the weld, all welds in this work failing at the faying surface between the two sheets (full interfacial failure).

### 3.3. Unloaded-crack samples

As opposed to the above *loaded crack* samples, the situation in *unloaded-crack* samples is depicted in Figure 8. The spot weld illustrated in Figure 8 contains a deep LME *outer* crack highlighted in red in the tomography slices. This particular crack (type A in AWS classification) is almost as deep as the sheet thickness.

Despite the presence of a (thin) LME *inner* crack in the loose end of the sheet in the tensile shear sample, the tomography setup used here did

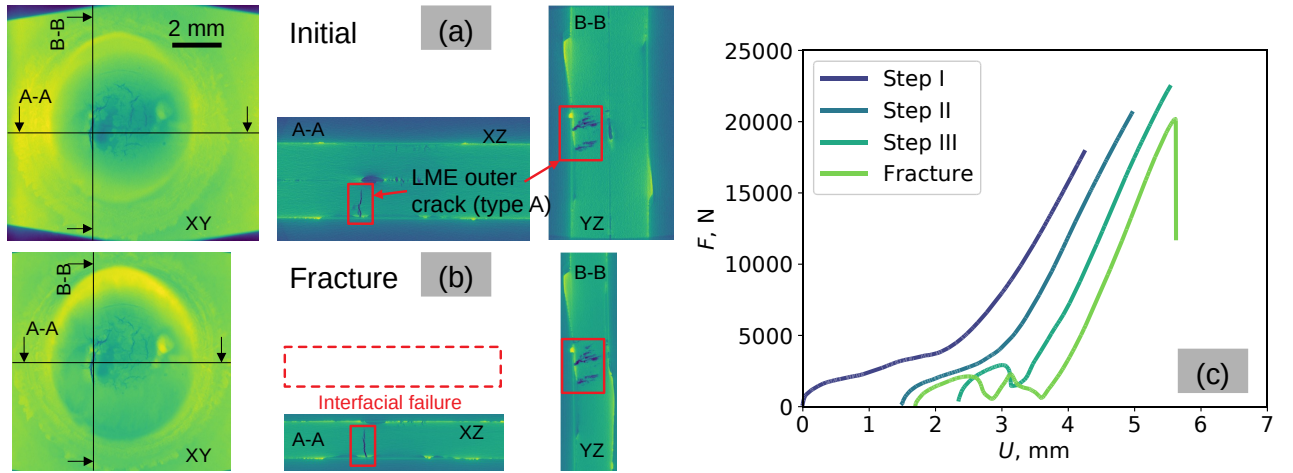


Figure 8: Unloaded-crack sample. a-b) Slices in the tomography volumes. c) Interrupted loading curves depicting the increasing load steps, where the curves are virtually shifted from each other for better readability. Final fracture occurs by full interfacial failure independently of the observed LME cracks.

not allow to detect it clearly in any of the four loading steps applied to the specimen (Figure 8.c). As a matter of fact, contrary to the situation described in section 3.2, the tensile load here does not contribute to open the LME inner crack, the latter remaining below the detection threshold (7 microns voxel size in the present setup).

Figure 8 shows that the huge LME *outer* crack remains unaffected during loading and the final fracture of the specimen occurs at the faying surface (full interfacial failure). A similar conclusion applies to the internal pores and to the LME *inner* crack that did not open and propagate during the test.

#### 4. Discussion

Section 3 illustrated the use of X-ray tomography as a non-destructive means for defect investigation in resistance spot welds. Internal pores and LME outer cracks could be observed in the welds from the initial state to the last stage of loading during *ex situ* tensile tests. Thin LME inner crack however could only be observed by tomography after some degree of pre-opening, when located at a position in the weld experiencing the tensile load directly. The authors emphasize the novelty of the present findings, this

study constituting the first one in the literature allowing to characterize and monitor 3D LME inner cracks in resistance spot welds during mechanical loading.

The topic of crack detection by X-ray tomography is a well-known problem in the context of fatigue testing of materials for example. As explained in Buffiere et al. [23], usual practice in this context consists in scanning the fatigue samples *in situ* under the maximum load, allowing for easier detection of the thin cracks. Moreover, samples specially designed for *in situ* testing in tomography present an optimized geometry: thin enough (i) to allow for transmission of the X-ray beam at every step of the sample rotation in the tomograph and (ii) to achieve the highest resolution of the 3D scan.

This illustrates the compromises that have to be met when trying to characterize real parts such as the resistance spot welds of the present study. In the present case, the load required to break welds did not allow for *in situ* tensile testing, hence requiring to load the welds *ex situ*. Moreover the 25 mm width of the samples could not be further reduced, unless significantly affecting the failure behavior of the tensile shear samples. A perspective in this context would consist in developing representative small-scale tensile shear samples of (small) resistance spot welds, which would allow for *in situ* tensile testing and easier detection of the different types of defects. This will be the topic of future work.

Another topic usually raised by such detailed investigation of a limited number of samples is the representativeness of the results. In the present work, special care was taken to remain in testing conditions close to the ones in ref. [12], where much more samples of the same material were tested and investigated by destructive metallographic cross sections mostly. In this context, the increased dispersion of mechanical properties measured in Siar et al. [12] in the presence of LME inner cracks indicates for example that differences in peak load observed on one single weld in Figure 6 (23.6 kN) or another one in Figure 8 (22.4 kN) is not statistically significant.

Nevertheless, as regards the global mechanical behavior of the welds under the presence of long LME inner cracks, the present study and the one in Siar et al. [12] reach the same conclusions by complementary means of investigations:

- LME inner cracks do not propagate unless located at a position in the tensile shear sample directly subjected to the tensile load.
- When directly subjected to the opening tensile load, the LME inner

cracks propagate in a stable way through the sheet thickness, which was characterized in 3D in Figure 6, but seldom affect the final crack path leading to the weld fracture.

- Most welds fail by full interfacial failure at the former faying surface, independently of the LME cracks. In Siar et al. [12], only 3 welds out of 30 containing LME inner cracks showed a final fracture path following the LME crack.

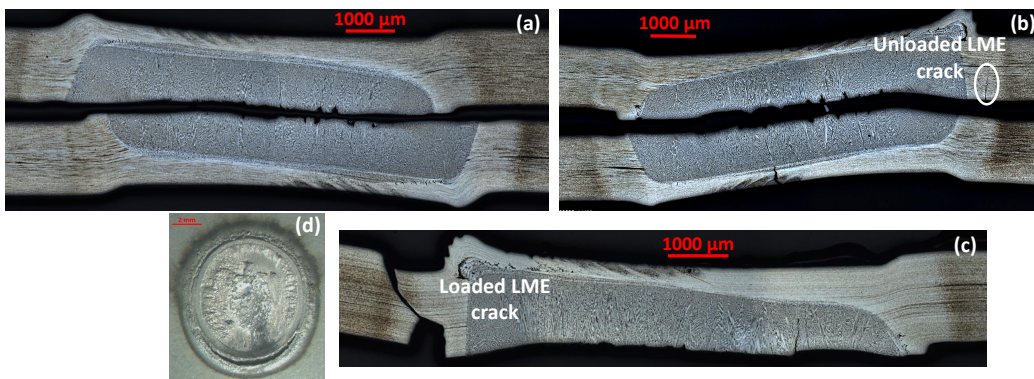


Figure 9: Metallographic observations of fractured samples: a) free of LME inner crack, b) with an unloaded LME inner crack, c) with a loaded LME inner crack. d) Top view of the fracture surface of the loaded-crack sample.

Such behavior in tensile shear is further illustrated in Figure 9 by means of metallographic cross sections obtained on the fractured spot welds of ref. [12]. Note that these welds were loaded to fracture without any interruption of loading. Figure 9 provides a similar overview of the fracture paths as the ones detailed in Figures 6 and 8 using the present interrupted X-ray tomography set-up. Namely, the weld without LME crack (Figure 9.a) shows interfacial crack propagation, which is also observed in the unloaded-crack sample of Figure 9.b. The inner LME crack of the latter remains unaffected by the tensile shear load. This is in contrast with the loaded-crack sample of 9.c that shows some stable propagation of the LME crack, but does not influence the final interfacial fracture path, as situation similar to the one described in Figure 6 in 3D.

This study provides additional evidence in 3D that the critical driving force for fracture in these welds remains the singularity of stress state at the notch tip around the weld nugget. When the critical value of stress

intensity factor (or toughness of the weld nugget) is reached, the notch tip crack propagates in an unstable way at the faying surface, leading to the well known interfacial failure type of resistance spot welds, as opposed to button pullout [28, 16, 17, 29]. It is worth noting that even when the inner LME crack is deep and critically loaded, its limited angular extension with respect to the full perimeter of the weld makes its propagation uncritical and has no impact on the fracture path nor on the weld final failure mode.

Several perspectives could be mentioned in this context in order to tune or favor one failure type or the other: adjusting the weld size and sample dimensions (sample width or sheet thickness) or tailoring the gradient of microstructures from the fusion zone to the base metal and the resulting local toughness of weld zones (e.g. post-welding heat treatment). Modifying the geometry of the samples alone, it is for example probable that reducing the sample width would favor at some point the localization of strain in the ligament ahead of the LME inner crack in a loaded-crack sample. This would therefore prevent the occurrence of full interfacial failure and allow investigating the inner LME crack involvement in the fracture path, when button pullout or partial interfacial failure modes occur.

## 5. Conclusion

An experimental procedure was developed to produce AHSS homogeneous resistance spot welds with significant LME inner cracks and characterize them in 3D by X-ray tomography. For the first time, their evolution was monitored *ex situ* in the course of tensile shear loading. The tomography setup allows to characterize internal pores and LME cracks in the welds with a voxel size of 7 microns. The thin LME *inner* cracks could however only be detected in loaded-crack samples, where the action of the tensile load directly operating on the crack helps slightly opening the crack lips. The evolution of the LME inner crack could be characterized in 3D in this case until complete propagation through the sheet thickness. Nevertheless, the final fracture of the specimens occurred at the faying surface in all welds investigated (full interfacial failure), independently of any LME crack.

## Acknowledgements

The authors would like to acknowledge fruitful discussions at Arcelor-Mittal with Y. Benlatreche about the experiments as well as careful reading

of the manuscript by B. Weber and D. Cornette. This research was funded by the ANRT (Association Nationale de la Recherche et de la Technologie, France), CIFRE grant number 2018/0962.

### Data availability

The raw/processed data required to reproduce these findings cannot be shared at this time as the data also forms part of an ongoing study.

### References

- [1] A. R. Marder, The metallurgy of zinc-coated steel, *Progress in Materials Science* 45 (2000) 191–271. doi:[https://doi.org/10.1016/S0079-6425\(98\)00006-1](https://doi.org/10.1016/S0079-6425(98)00006-1).
- [2] C. Beal, X. Kleber, D. Fabregue, M. Bouzekri, Liquid zinc embrittlement of twinning-induced plasticity steel, *Scripta Materialia* 66 (2012) 1030–1033. doi:<https://doi.org/10.1016/j.scriptamat.2011.12.040>.
- [3] W.-S. Jeon, A. Sharma, J. P. Jung, Liquid metal embrittlement of galvanized TRIP steels in resistance spot welding, *Metals* 10 (2020). doi:10.3390/met10060787.
- [4] AWS, AWS D8.9M:2012 Test methods for evaluating the resistance spot welding behavior of automotive sheet steel materials, 2012. URL: <https://pubs.aws.org/p/1067/d89m2012-test-methods-for-evaluating-the-resistance-spot-welding-behavior-of-automotive-sheet-steel-materials>.
- [5] H. Gaul, G. Weber, M. Rethmeier, Influence of HAZ cracks on fatigue resistance of resistance spot welded joints made of advanced high strength steels, *Science and Technology of Welding and Joining* 16 (2011) 440–445. doi:10.1179/1362171810Y.0000000031, publisher: Taylor & Francis.
- [6] S. Brauser, C. Schwenk, M. Rethmeier, T. Noack, S. Jüttner, Influence of welding-induced cracks on the fatigue strength of resistance-spot-welded joints made of high-strength austenitic steel, *Welding and cutting* 11 (2012) 232–235. Place: Düsseldorf Publisher: DVS - German Welding Society.

- [7] Y. G. Kim, I. J. Kim, J. S. Kim, Y. I. Chung, D. Y. Choi, Evaluation of surface crack in resistance spot welds of zn-coated steel, *MATERIALS TRANSACTIONS advpub* (2014). doi:10.2320/matertrans.M2013244.
- [8] D.-Y. Choi, S.-H. Uhm, C. M. Enloe, H. Lee, G. Kim, C. Horvath, Liquid metal embrittlement of resistance spot welded 1180trip steel - effects of crack geometry on weld mechanical performance, *Mater. Sci. Technol.* (2017) 454–462.
- [9] C. DiGiovanni, E. Biro, N. Y. Zhou, Impact of liquid metal embrittlement cracks on resistance spot weld static strength, *Science and Technology of Welding and Joining* 24 (2019) 218–224. doi:10.1080/13621718.2018.1518363, publisher: Taylor & Francis.
- [10] Y. Benlatreche, M. Duchet, T. Dupuy, D. Cornette, G. Carollo, Effect of liquid metal embrittlement cracks on the mechanical performances of spot welds, in: *5th International Conference on Steels in Cars and Trucks*, 2017.
- [11] Y. Benlatreche, Ghassemi-Armaki, M. Duchet, T. Dupuy, D. Cornette, G. Carollo, P. Dietsch, Spot-weld integrity of zn-coated 3rd gen. advanced high strength steels in presence of LME, in: *IABC2017 – International Automotive Body Congress 2017*, 2017.
- [12] O. Siar, S. Dancette, T. Dupuy, D. Fabregue, Impact of Liquid Metal Embrittlement inner cracks on the mechanical behavior of 3rd generation Advanced High Strength Steel spot welds, *Journal of Materials Research and Technology*, in press (2021) 29. doi:10.1016/j.jmrt.2021.11.100.
- [13] K. Kwon, G. Jang, W. Kim, S. Uhm, T. Lee, C. S. Lee, Effect of type-C liquid metal embrittlement on mechanical properties of spot-welded TRIP steel, *Journal of Materials Research and Technology* (2021) S2238785421005962. URL: <https://linkinghub.elsevier.com/retrieve/pii/S2238785421005962>. doi:10.1016/j.jmrt.2021.06.041.
- [14] O. Siar, Y. Benlatreche, T. Dupuy, S. Dancette, D. Fabrègue, Effect of severe welding conditions on liquid metal embrittlement of a 3rd-generation advanced high-strength steel, *Metals* 10 (2020). doi:10.3390/met10091166.

- [15] M. Bouzekri, S. Dancette, T. Dupuy, A. Lens, B. Nait Oultit, V. Massardier, D. Fabregue, H. Klöcker, An investigation of failure types in high-strength steel resistance spot welds, *Welding in the World* 54 (2010) 12.
- [16] S. Dancette, D. Fabrègue, V. Massardier, J. Merlin, T. Dupuy, M. Bouzekri, Experimental and modeling investigation of the failure resistance of Advanced High Strength Steels spot welds, *Engineering Fracture Mechanics* 78 (2011) 2259–2272. doi:10.1016/j.engfracmech.2011.04.013.
- [17] S. Dancette, D. Fabrègue, V. Massardier, J. Merlin, T. Dupuy, M. Bouzekri, Investigation of the Tensile Shear fracture of Advanced High Strength Steel spot welds, *Engineering Failure Analysis* 25 (2012) 112–122. doi:10.1016/j.engfailanal.2012.04.009.
- [18] T. Huin, S. Dancette, D. Fabrègue, T. Dupuy, Investigation of the failure of advanced high strength steels heterogeneous spot welds, *Metals* 6 (2016). doi:10.3390/met6050111.
- [19] Y. Benlatreche, T. Dupuy, H. Ghassemi-Armaki, L. Lucchini, Methodology for liquid metal embrittlement (LME) evaluation of coated steels during spot welding, in: *The 72nd annual assembly of the International Institute of Welding (IIW)*, 2019.
- [20] C. DiGiovanni, L. He, C. Hawkins, N. Zhou, E. Biro, Significance of cutting plane in liquid metal embrittlement severity quantification, *SN Applied Sciences* 3 (2021) 620. doi:https://doi.org/10.1007/s42452-021-04608-2.
- [21] D. Bhattacharya, Liquid metal embrittlement during resistance spot welding of zn-coated high-strength steels, *Materials Science and Technology* 34 (2018) 1809–1829. doi:10.1080/02670836.2018.1461595, publisher: Taylor & Francis \_eprint: https://doi.org/10.1080/02670836.2018.1461595.
- [22] E. Maire, P. J. Withers, Quantitative X-ray tomography, *International Materials Reviews* 59 (2014) 1–43. URL: <http://www.maneyonline.com/doi/abs/10.1179/1743280413Y.0000000023>. doi:10.1179/1743280413Y.0000000023.

- [23] J. Y. Buffiere, E. Maire, J. Adrien, J. P. Masse, E. Boller, In Situ Experiments with X ray Tomography: an Attractive Tool for Experimental Mechanics, *Exp Mech* 50 (2010) 289–305. doi:10.1007/s11340-010-9333-7.
- [24] S. Hang, H. Park, S. Uhm, Evaluation of liquid metal embrittlement crack in resistance spot welds under intensive welding condition using industrial x-ray computed tomography and machine learning, *Welding in the World* (2021). doi:https://doi.org/10.1007/s40194-021-01109-z.
- [25] ISO5821, Soudage par résistance — Embouts amovibles de pointes d'électrodes pour soudage par points ISO 5821, 2009.
- [26] T. Ferreira, W. Rasband, The imagej user guide: Ij 1.46r (2012). doi:https://doi=10.1.1.731.215.
- [27] A. H. Squillacote, The paraview guide: A parallel visualization application (2007). doi:https://doi/abs/10.5555/2789330.
- [28] Y. J. Chao, Failure mode of spot welds: interfacial versus pullout, *Science and technology of welding and joining* 8 (2003) 133–137.
- [29] S. Dancette, T. Huin, T. Dupuy, D. Fabrègue, Finite element modeling of deformation and fracture of advanced high strength steels dissimilar spot welds, *Engineering Fracture Mechanics* (2021) 108092. doi:10.1016/j.engfracmech.2021.108092.